Gleeble Physical Simulation of High-Frequency Induction Welding of TRIP 690

Physically simulating the high-frequency induction welding of thin TRIP 690 steel typically used for automotive tubular applications in a Gleeble 3500 simulator

BY S. FAIQUE AL HUSSAIN, A. SHAFIEE, S. OKOROAFOR, D. C. RAMACHANDRAN, A. SALANDARI-RABORI, M. SHOJAEE, D. ODOH, AND E. BIRO

Abstract

High-frequency induction welding (HFIW) is the predominant process used to weld strip edges during the production of automotive structural tubing. The high-throughput nature of HFIW makes it ideal for welding advanced high-strength steel tubes; however, oxides containing Al, Mn, and Si can sometimes form along the strip edges and become entrapped within the weld bond line. In welds containing oxide inclusions, the strength and ductility of the weld joint will be significantly decreased. High operational costs of running a tube make it difficult to determine favorable conditions for oxide inclusion formation through mill trials. This study shows that the Gleeble was capable of providing insights on appropriate welding temperatures to achieve defect-free HFIW in TRIP 690. The simulated samples reproduced the bond line and heat-affected zone microstructures of the industrially produced HFIW welds. Mechanical characterization revealed similar hardness distribution across the Gleeble and HFIW welds. Notably, bond line oxide inclusions, such as those found in HFIW tubes, were also observed in the simulated welds. The effects of these inclusions on tensile properties and fracture mechanisms in industrial and simulated welds were determined, and ideal conditions for producing oxide-free welds to ensure superior weld mechanical properties were determined.

Keywords

- High-Frequency Induction Welding
- Gleeble Simulation
- Oxide Inclusions
- Weld Quality
- Process Optimization
- Bond Line Defects

Introduction

High-frequency induction heating has been used since 1944 (Ref. 1). In the 1960s, high-frequency induction heating was applied to pipe and tube welding in a process known as high-frequency induction welding (HFIW) (Ref. 2). Since then, HFIW has become a staple process for large-scale production of closed-seam pipes and tubes made from advanced high-strength steels (AHSS) (Ref. 3). HFIW is ideal for large-scale industrial production of such tubes for several reasons, such as high throughput, continuous nature, capability of welding large quantities of tubes, and its ability to weld a wide variety of tube sizes (Ref. 4).

Transformation-induced plasticity (TRIP) steel is a first-generation multiphase AHSS with a microstructure comprising retained austenite and ferrite. The high strength-to-weight ratio and excellent high-strain-rate behavior contribute to overall weight savings and improved crash-worthiness, respectively, making TRIP steels widely applied in the automotive industry. These properties can be traced to the TRIP effect, in which material strain causes retained austenite to transform into martensite in the microstructure (Refs. 5–7). Oliver et al. (Ref. 8) reported that TRIP steels exhibit superior formability and greater energy absorption at low and high strength in comparison with dual-phase steels with comparable tensile strength. However, previous studies

https://doi.org/10.29391/2026.105.017

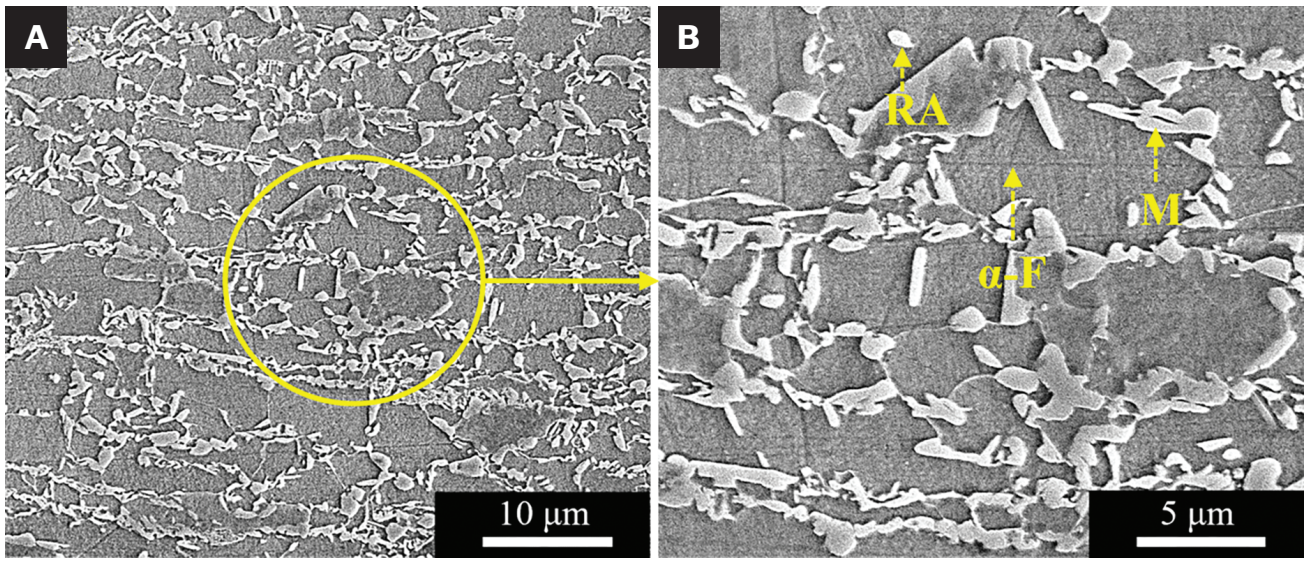


Fig. 1 — Base material microstructure of TRIP 690.

Table 1 — Chemical Composition of TRIP 690 Steel Used for Simulation

C	Mn	Al	Si	Cr + Mo + Ti + V
0.23	1.6	1.5	0.1	0.04

have shown that during HFIW, the bond line (BL) of Mn-Si-Al TRIP steels is susceptible to forming nonmetallic oxide inclusions containing Mn, Al, and Si (Refs. 9, 10). The presence of these oxide inclusions along the BL negatively impacts the mechanical performance of the weld (Refs. 2, 11, 12).

The high-speed continuous nature of the HFIW process makes in-situ weld quality monitoring difficult, and mill trials are costly and impractical due to high material usage. This requires developing laboratory-scale simulations to understand HFIW. Early investigation (Ref. 13) attempted to analyze the process analytically; however, the coupled electrical, thermal, metallurgical, and mechanical effects made it difficult to use analytical solutions for process design. The complexity of the process has led to significant research using numerical methods to simulate it (Refs. 14–23). Even though some HFIW mechanisms may be clarified through numerical simulation, there remains a need to verify and validate the boundary conditions and results of these simulations using inexpensive experimental methods.

Compared with numerical simulations, there is limited research on lab-scale physical simulations of the HFIW. The first reported physical simulation of HFIW was by Santana et al. (Ref. 24), where HFIW of stainless steels was conducted using modified spot welding equipment. In this study, simulated welds with similar strength and microstructure to industrial HFIW welds were produced, but parameters such as peak temperature, stroke rate, and stroke amount were not measured. In 2020, Kannan et al. (Ref. 25) used a Gleeble thermomechanical simulator to physically simulate HFIW of 6-mm-thick cylindrical samples of X70 pipeline steel. Through this study, they presented a mechanism for the formation of a carbon-depleted bond line found in HFIW samples and showed that physical simulation using a Gleeble is viable. However, the authors (Ref. 25) did not investigate bond line oxide inclusions or conduct mechanical testing on their simulated welds. The possibility of using the Gleeble to simulate HFIW of automotive sheet steels, which are thinner and welded at much higher welding speeds, was not explored in that study. Finally, Egger et al. (Ref. 12) physically simulated the HFIW process in 3.5-mm annealed 34MnB5 steel sheets using a custom-designed electro-thermo-mechanical apparatus that conductively heated tube welds. This is the most comparable simulation of the HFIW process, as the equipment uses a power-controlled induction heater, and mechanisms such as the proximity and skin effects are observed. Through this study, Egger et al. (Ref. 12) determined the relationship between weld parameters and mechanical properties of the resulting weld. While Egger et al. (Ref. 12) investigated the effect of bond line oxide inclusions on weld strength, they observed only cold-welding oxides (formed due to insufficient heat input) and did not validate their results with commercially welded tubes.

The objective was to physically simulate the HFIW of thin TRIP 690 steel typically used for automotive tubular applications in a Gleeble 3500 simulator. The physical simulation technique will enable future offline welding trials to optimize HFIW parameters and produce high-quality oxide-free welds. Experimental trials were conducted using a Gleeble to determine suitable welding temperatures for solid-state welds. Welds were characterized metallographically and mechanically, with an emphasis on examining the bond line oxides. The Gleeble-made welds were compared with industrially

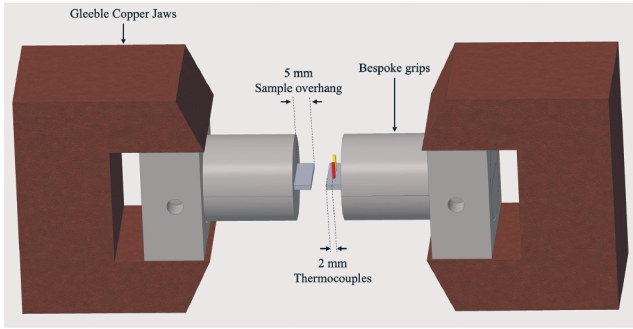


Fig. 2 — Schematic diagram of the experimental setup used for Gleeble simulations.

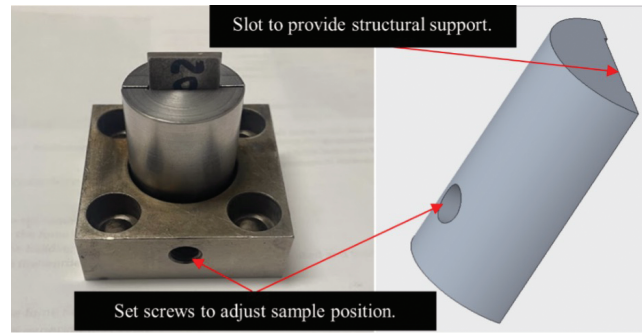


Fig. 3 — Gleeble grips designed to eliminate buckling and misalignment.

Table 2 — Input and Output Temperatures and Stroke Values for Gleeble Study

Trial Number	Set Thermocouple Temperature (2 mm from edge)	Input Stroke (Squeeze)	Peak Temperature at Bond Line (IR Camera)	Stroke Achieved
T1	1310°C	1.54 mm	1410°C	1.48 mm
T2	1330°C	1.26 mm	1439°C	1.20 mm
T3	1330°C	1.54 mm	1474°C	1.50 mm
T4	1350°C	1.40 mm	1486°C	1.38 mm
T5	1350°C	1.26 mm	1471°C	1.20 mm
T6	1310°C	1.40 mm	1473°C	1.44 mm
T7	1310°C	1.26 mm	1502°C	1.17 mm
T8	1350°C	1.54 mm	1569°C	1.42 mm
T9	1330°C	1.40 mm	1504°C	1.35 mm
T10	1360°C	1.40 mm	1507°C	1.42 mm

produced HFIW welds to assess the validity of the physical simulation technique.

Experimental Procedure

Base Material and Welding Coupon Preparation

The material used in this study was 1.3-mm-thick TRIP 690. It had a predominantly ferritic (α-F) microstructure with small fractions of martensite (M) and retained austenite (RA), as seen in Fig. 1. Its chemical composition may be found in Table 1. Similar to most TRIP steels, it was very hardenable, having a carbon equivalent of 0.511, calculated using Yurioka et al.'s method (Ref. 26). Coupons for Gleeble thermo-mechanical simulation were cut to 15 × 50 mm using a ProtoMAX waterjet cutter. The welding edge (15 mm) was oriented parallel to the rolling direction to match the production-made welds. Zn coating was removed from all samples to prevent thermocouple detachment during processing by immersing samples in 35% hydrochloric acid for 50 s, followed by a methanol rinse to halt the acid-metal reaction. The edges to be welded and thermocouple locations were then ground using 400-grit sandpaper. Finally, the samples were cleaned using methanol to remove any remaining contamination.

Gleeble Simulation

Thermocouples (K-type, 0.25 mm diameter) were welded 2 mm away from the welding edge of one of the coupons, parallel to the edge. The two thermocouple wires were spaced 2 mm apart, centered on the coupon's midline (Fig. 2). The coupons were then secured in custom-made stainless-steel

grips (Fig. 2). Welding was imaged using a short-wave infrared (IR) thermal imaging camera (XIRIS Automation XIR-1800). Temperature measurements with the IR camera were taken from the top surface of the bond line, using an emissivity of 0.67. Previous work has shown that these measurements have an accuracy of ± 12.9°C (Ref. 27). As the thermocouples were only used to control the Gleeble and not used to evaluate the weld bond line temperature, the inaccuracies associated with using K-Type thermocouples outside of their calibrated temperature range did not affect the temperature analysis from this work.

During Gleeble processing, temperature (at the thermocouples), stroke, preload, heating rate, and stroke rate were controlled. A heating rate of 1000°C/s and a stroke rate of 22.5 mm/s were used throughout the experiment, providing a balance between matching the mill conditions and remaining within the Gleeble's controllable limits. Due to the continuous nature of the HFIW process and the batch nature of Gleeble welds, the Gleeble parameters must be transformed to determine the continuous welding parameters. Such transformations have been reported previously (Ref. 28). The parameters were monitored at a data-acquisition frequency of 2000 Hz. The welding sequence started with the application of a preload, followed by current application until the peak temperature was achieved, then weld upset (application of stroke) to create the solid-state weld. Experimental parameters were chosen so that the bond line temperature (greater than the thermocouple temperature) ranged between the sample's solidus and liquidus (1472°C and 1516°C, respectively, as calculated using JMatPro v14.1), and the stroke ranged between 90 and 110% of the sheet thickness. It should be noted that in the T8 case, the bond line temperature exceeded the material's melting point. The full list of experimental parameters is presented in Table 2. The peak temperature at bond line and the stroke achieved were measured results from the test and were not experimental parameters.

Sample Preparation and Microscopy

Metallographic cross sections were taken perpendicular to the welds. Weld sections were cut using an abrasive saw and hot-mounted in Struers Polyfast conductive resin. The mounted samples were polished to a 1 µm grit diamond finish using standard metallographic techniques. Once polished, samples were cleaned using methanol and etched with 5% Nital solution for 5 s in preparation. Optical and scanning electron microscopy (SEM) were performed using a Keyence VHX digital microscope and a Quanta 200 FEG E-SEM with energy-dispersive spectroscopy (EDS), respectively.

Hardness Testing

Vickers microhardness testing was conducted across the base metal, heat-affected zone (HAZ), and BL using a Clemex CMT-LC Hardness Tester. All indents were made using a 100 g force. The microhardness profile was conducted horizontally at a quarter of the sheet thickness from the top edge (see Fig. 4). In the base metal and HAZ region, horizontal spacing of 150 micrometers was used between each indent. To increase measurement resolution across the narrow BL 20-40 µm wide (Ref. 29), the horizontal spacing was reduced to 75 µm, and additional indents were placed at a vertical offset of 150 µm and a horizontal offset of 37.5 µm relative to the original indents. This pattern ensured that indents were spaced at least 2.5 times their diameter apart, in compliance with ASTM E384-22 (Ref. 30).

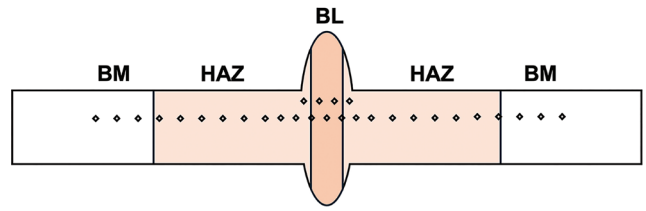


Fig. 4 — Hardness profile schematic on cross-sectioned weld showing offset points on BL.

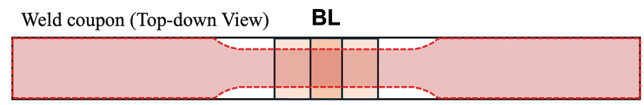


Fig. 5 — Schematic of subsize tensile coupon milled out from Gleeble-welded coupon.

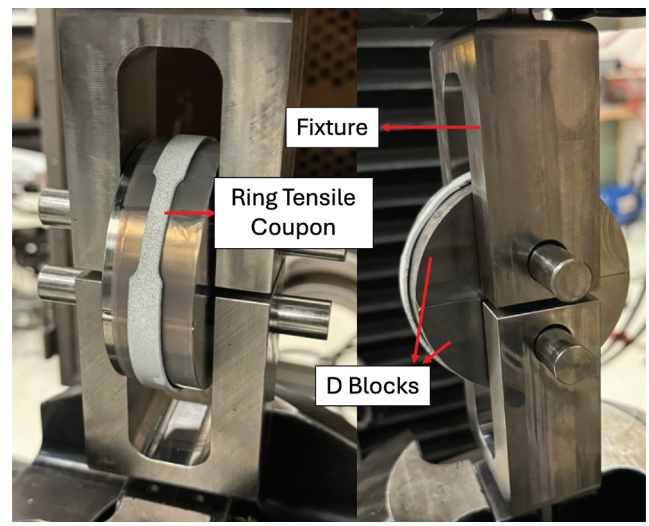


Fig. 6 — RHTT experimental setup showing fixtures, semicircular D blocks and subsize tube tensile coupon (Ref. 35).

Tensile Testing

Tensile coupons were machined from the Gleeble welds based on ASTM E-8 (Ref. 31) subsize tensile coupons (see Fig. 5). The weld was positioned in the center of the gauge length and oriented perpendicular to the tensile load. Squeezed-out material from the bond line was removed by using wire electrode discharge machining prior to tensile testing. Tensile tests were performed at a crosshead speed of 1 mm/s on a Shimadzu AG-X universal testing machine with a 50 kN

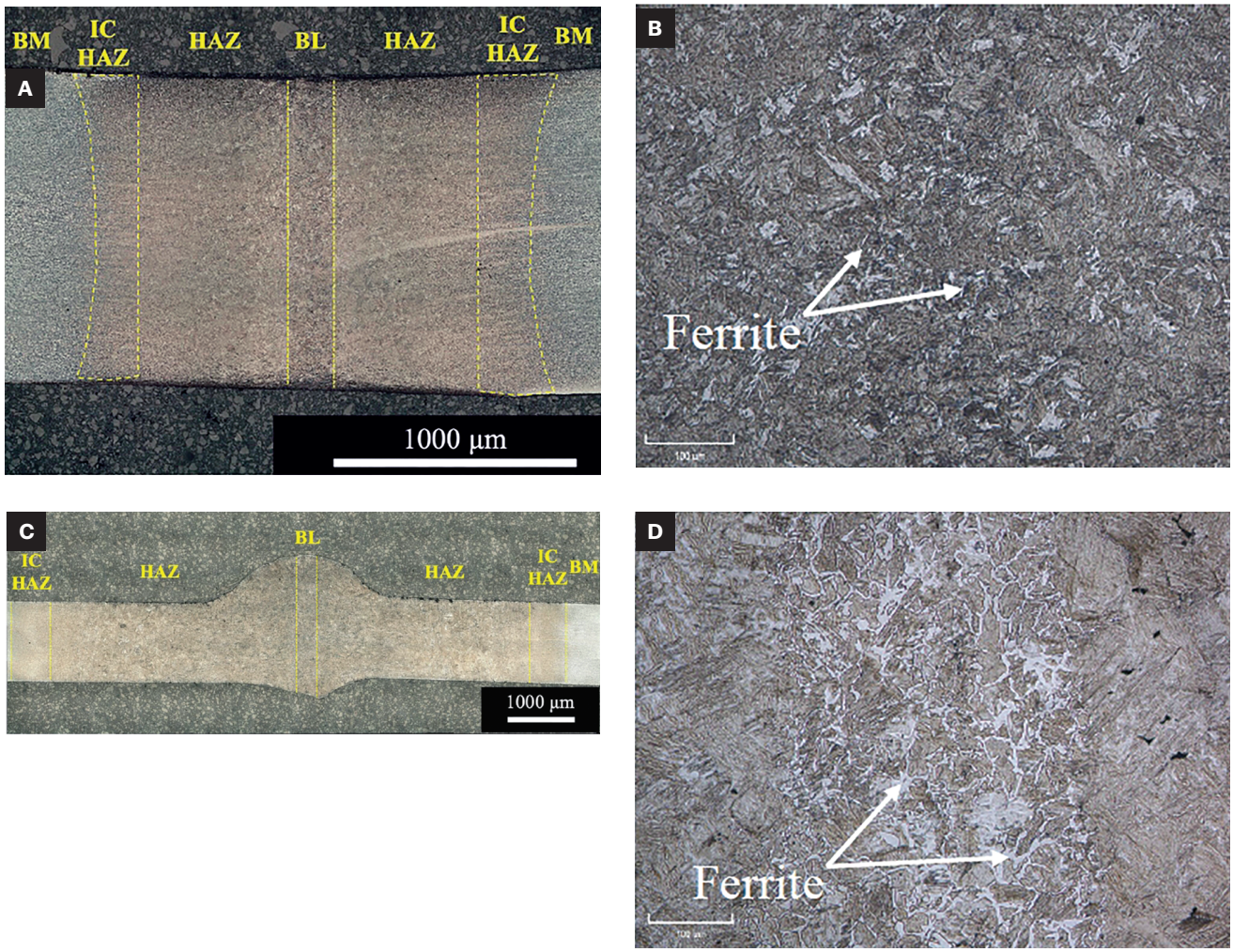


Fig. 7 — Optical macrographs showing the cross sections from the HFIW at: A — Low magnification; B — high magnification of the BL; C — low magnification image of the Gleeble weld; D — high magnifications image of its bond line.

load cell. Two 3D Digital Image Correlation (DIC) cameras were used to monitor the strain, and the data was processed using VIC 3D.

Ring Hoop Tensile Testing

The ring hoop tensile test (RHTT) allows tensile testing of tubes in the hoop direction while preserving the tube radius. RHTT was performed on circumferential coupon samples extracted from the tubes welded through an industrial HFIW process (Refs. 32–34). The tensile strength of these samples was subsequently compared to that of the Gleeble-welded samples. The fixtures and circular D blocks were both manufactured from 4140 tool steel (Ref. 35) (Fig. 6). The reduced section of the RHTT samples was oriented so the weld was located in the center of the gauge length, and the reduced area conformed to the ASTM E-8 subsize standard. All reported tolerances represent the 95% confidence interval.

Results

Microstructure

The microstructure of industrially produced HFIW tube welds was examined to compare with that of Gleeble welds. The HFIW tube welds had a narrow, hourglass shaped weld zone that was 3.8 mm wide with distinct HAZ and BL regions (Fig. 7A). Gleeble made welds exhibited the same regions as the production welds, but Gleeble welds were wider (11.4 vs. 3.8 mm) with a consistent (nonhourglass) appearance, as shown in Fig. 7C. The increased width of the Gleeble samples is attributed to the bulk heating of the Gleeble sample, resulting from current (60 Hz AC) flowing along its length (perpendicular to the weld) heating entire sample length, unlike the HFIW process heated using high frequency (400 kHz) AC current flows predominantly along the strip edge surface due to the skin and proximity effects, localizing heating, resulting in an hourglass appearance (Ref. 3).

The HFIW tubes and Gleeble-welded samples generally had the same HAZ and BL microstructures (see Fig. 7). The

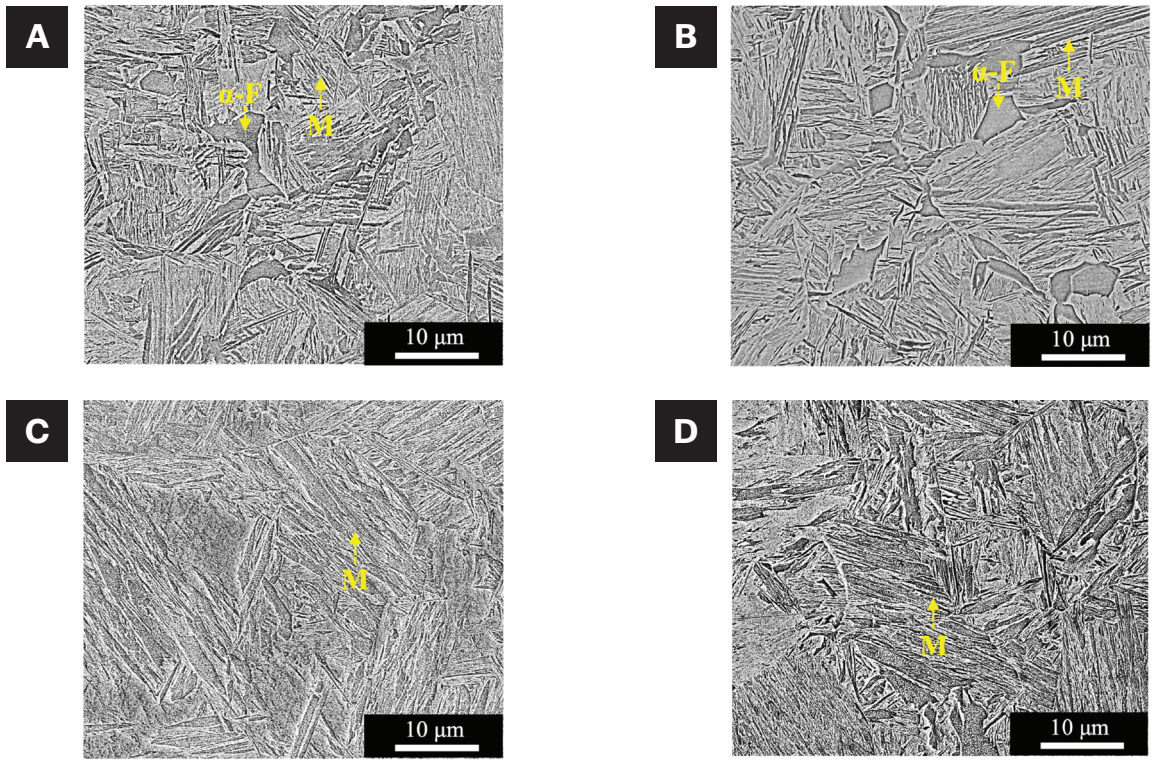


Fig. 8 — SEM micrographs at 200× magnification of: A — HFIW BL; B — Gleeble BL; C — HFIW HAZ; D — Gleeble HAZ.

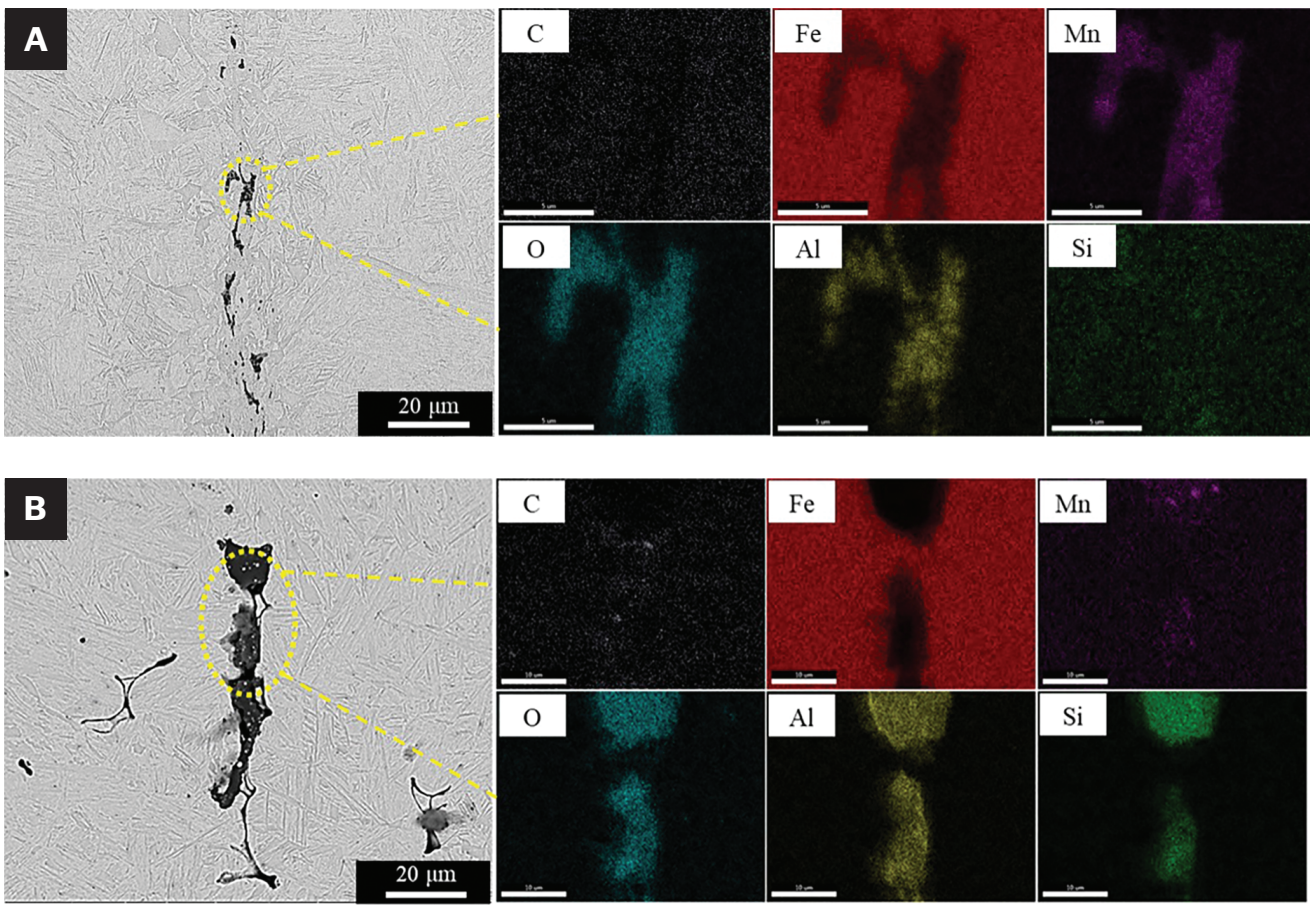


Fig. 10 — Different brightness conditions: A to C — Original weld bead images; E to F —their segmented results.

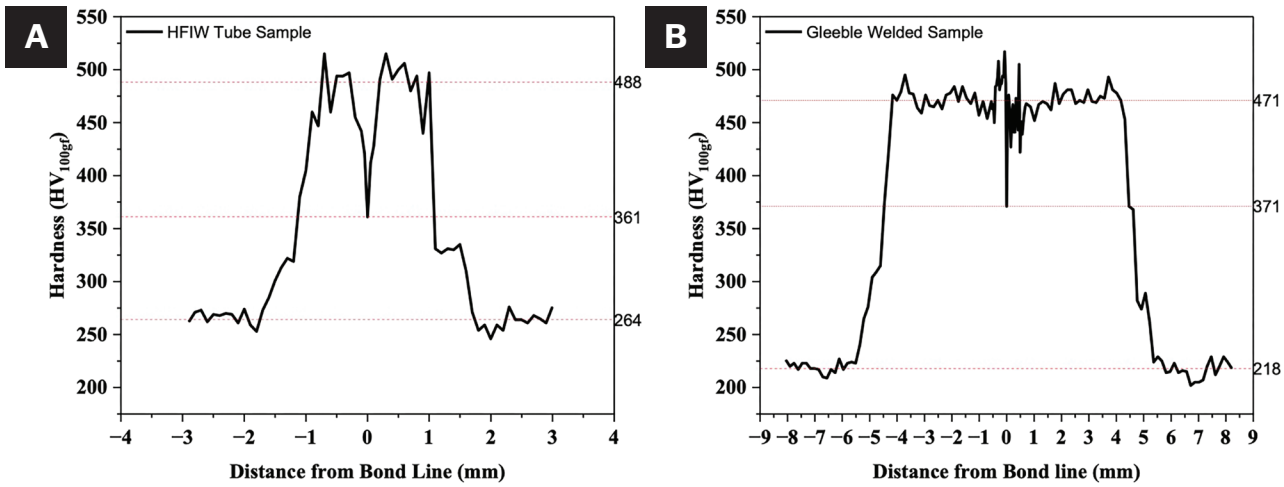


Fig. 10 — Hardness profile for: A — HFIW tube sample; B — Gleeble-welded sample.

BL microstructure of the HFIW and Gleeble welds contained α-ferrite with lath martensite and some tempered martensite/bainite. Microstructural similarities are due to similarity in bond formation, where the BL region is heated to a semisolid state consisting of δ-ferrite and liquid. Due to C partitioning, the liquid has a higher C content than the remaining solid. On forging, the molten metal is squeezed from the bond line, resulting in a low-C solid in the BL that transforms into a mixture of α-ferrite, martensite, and tempered martensite/bainite on cooling (Refs. 25, 36). Due to the high hardenability of the material used in this study, the white BL, typically observed (Ref. 36), was not prominent because the BL was highly martensitic. At high magnification, the BL had more ferrite than the surrounding HAZ, due to the locally lower C content. This was more evident along the BL of the Gleeble weld (Fig. 7D) than the tube weld (Fig. 7B) due to the higher cooling rate during HFIW. The HAZ microstructure is similar in both welds, consisting almost entirely of lath martensite.

Comparison of BL Oxide Inclusions in HFIW and Gleeble-Welded Samples

Some of the HFIW tube samples contained dark features within the BL. EDS maps of these features (Fig. 9A) showed that they had decreased Fe and C, and increased Al, Mn, and O. Thus, they are likely Al- and Mn-containing oxides. These oxide inclusions were ~ 5-10 µm wide and ~ 60 µm long (through-thickness direction) along the tube BL. Oxide inclusions were also found along the BL of some of the Gleeble welds (see Fig. 9B). The oxides found in the Gleeble welds were larger and less dispersed than those in the HFIW welds. The chemical composition of the oxides also differed slightly. The oxides in the Gleeble welds contained Al and Si, whereas HFIW oxides contained Al and Mn. This variation is likely due to the difference in the timing of the HFIW and Gleeble welding processes. Significantly higher heating rates in the HFIW tube mill (~ 15,000°C/s in the vee, measured using Xiris thermal camera), resulting in much shorter oxidation times than during Gleeble welding.

Microhardness

Generally, the characteristics of hardness profiles in the HFIW and Gleeble welds were similar, once differences in weld dimensions were accounted for, with hardness peaking across the HAZ and decreasing at the BL (Fig. 10). However, there were small local differences between the welds. In HFIW samples, the average hardness of the base material (BM) was 259 HV ± 2 HV as compared to 227 HV ± 1 HV in the Gleeble-welded samples. This was likely due to work-hardening of the tube mill's fin-pass rolls' edges prior to welding. The HAZ region had an average hardness of 492 HV ± 6 HV and 469 HV ± 2 HV in the HFIW tube and Gleeble-welded samples, respectively. The higher hardness of the HAZ in the HFIW samples may be due to the retention of a higher dislocation density from work hardening during tube forming; however, a detailed understanding of this was beyond the scope of the study. The BL of the Gleeble welds showed a similar hardness drop observed in the BL of HFIW tube welds, due to the C partitioning during heating described previously (Ref. 36). The average BL hardness was 372 HV ± 19 HV and 396 HV ± 15 HV for the HFIW and Gleeble samples, respectively.

Tensile Testing

The strength of the HFIW tube welds was measured from three replicates cut from 4 different locations on the HFIW tube (12 samples total). RHTT tensile results from the 12 samples are seen in Fig. 11. Eight of the samples failed in the base metal with elongation ranging between 20-22%, and the remaining samples failed in the BL with lower UTS (630.8 to 730.6 MPa) and elongation values ranging between 2 to 10.8%. DIC obtained strain evolution curves for all the samples (Fig. 12), showing strain initially accumulated in the base metal, after which strain localization occurred, leading to an asymmetrical strain evolution pattern (Fig. 12A) for samples exhibiting BM failures. However, for samples failing along the BL, sudden failure at the BL occurred without apparent necking (Fig. 12B). The strain spike (red

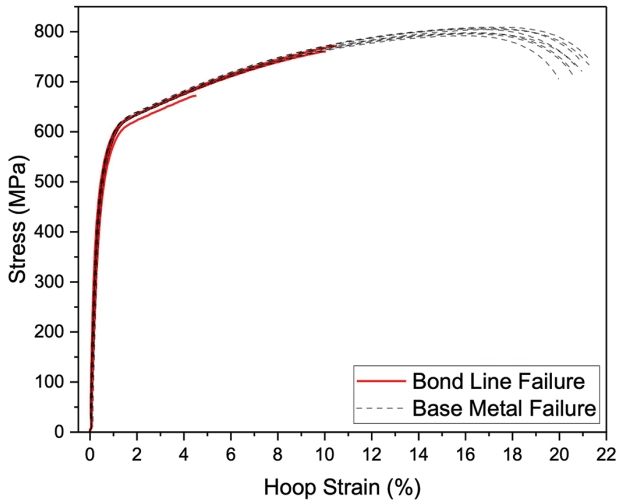
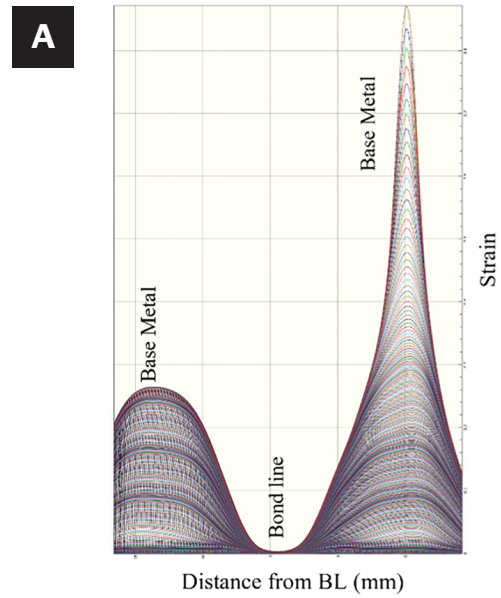


Fig. 11 — Tensile testing results for coupons extracted from tube samples.



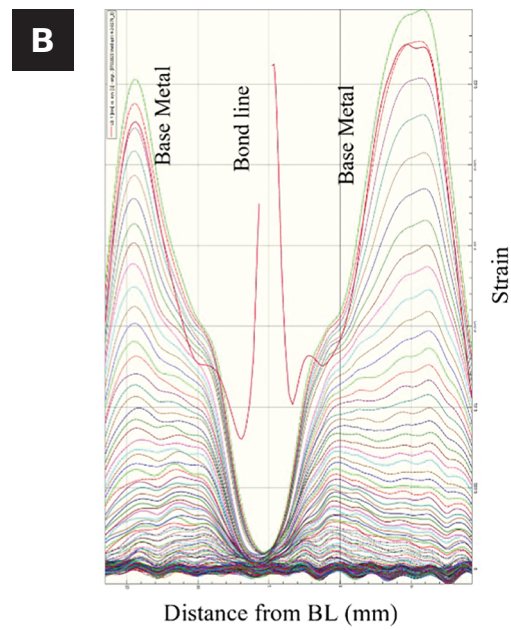


Fig. 12 — DIC obtained strain evolution curves for tensile coupons extracted from HFIW tube welded samples: A — RHTT failing in the BM; B — samples failing along the BL.

line) seen on the last measurement is due to the opening of the sample after failure.

A total of 10 sub-size tensile coupons were milled from the Gleeble-welded samples. The strengths of the Gleeble-welded specimens were similar to those of the industrial HFIW tubes. Most of the Gleeble-welded samples failed in the BM; only 2 failed in the BL. Gleeble tensile samples failing in the BM showed a larger variation in elongation values than seen in the HFIW samples (see Fig. 13). Tensile testing result of the Gleeble weld samples may be separated into three categories: Runs T1-T6 failed in the BM with elongation between 16 and 19% and average UTS of 754 MPa (Type A); runs T7 and T8, also failed in the BM, with reduced elongation (12-14%) and an average UTS of 726 MPa (Type B); and runs T9 and T10 that failed along the BL with extremely low elongation ($\leq$ 1%) and average UTS (404 MPa), which is noted as Type C.

DIC strain evolution maps of the Gleeble-welded samples showed similar trends to those seen during RHTT of samples extracted from the industrial HFIW welds (see Fig. 14). For Type A and B failure samples, the strain curves show uniform straining in the BM region with strain localization occurring only on one side of the weld. The initial strain distribution in samples exhibiting Type C failure was uniform in the BM. However, a sudden spike in strain was then observed in the BL region of Type C samples, leading to failure within the BL.

Discussion

Fracture Surface Analysis

The fracture surface from the Gleeble-welded sample extracts exhibiting identified failure types were examined using SEM. Inclusions were not observed on the surface of samples exhibiting Type A failure, which was expected as failure occurred in the BM (see Fig. 15A). As seen at higher magnification (Figs. 15B and C), microvoid coalescence (MVC), indicating failure occurred by ductile overload (Ref. 37). Likewise, samples that exhibited Type B failure also exhibited MVC, indicating failure by ductile overload (see Fig. 16).

There are no obvious differences in the fracture faces of the welds exhibiting Type A and B failures, but there are nonfracture-related hypotheses explaining the reduced elongation of the samples exhibiting Type B failure. The first explanation is that the weld width of the Type B failure exhibiting samples was likely greater than that of exhibiting Type A failure, as the Type B failure exhibiting samples were welded at higher temperatures (1502°C and 1569°C). Examination of the local strain data during testing showed little to no strain accumulated in the welded region during tensile testing for samples exhibiting either Type A or B failures (Fig. 14). As a

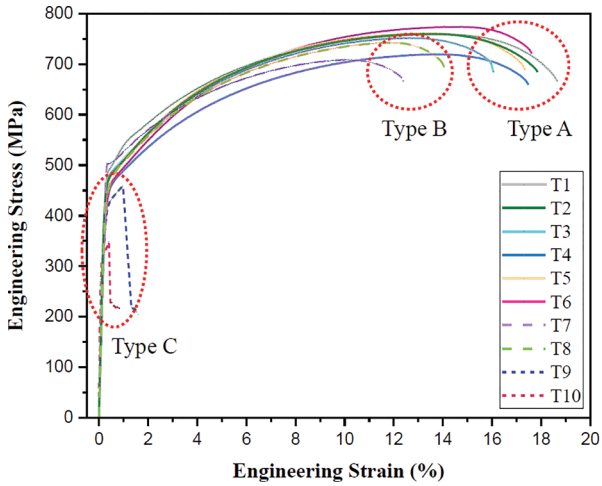


Fig. 13 — Gleeble-welded samples tensile test results for type: A — Solid lines; B — dashed lines; C — short dashes.

wider weld region takes up a higher percentage of the 33.1 mm gauge length (the sample with the highest observed weld width takes up 37.5% of the gauge length), there is less BM subjected to local straining, so the increase in the overall virtual gauge length during the test will be less than a weld with a narrower weld zone. A second possibility is that the base metal of the samples exhibiting Type B failure were hardened during prior material handling/processing (some sheets were flattened to remove coil set prior to sample preparation). This may explain why the average UTS of samples with Type B failures were 3.6% lower than samples with Type A failures. Further work is required to fully understand what is responsible for the reduced elongation associated with Type B failure.

Unlike samples with Type A and Type B failures, samples with Type C failure fractured at the BL with very low elongation. When the fracture surface was examined using the SEM, many dark features were seen on the fracture surface (Fig. 17A). There is very little MVC seen in the fracture surface

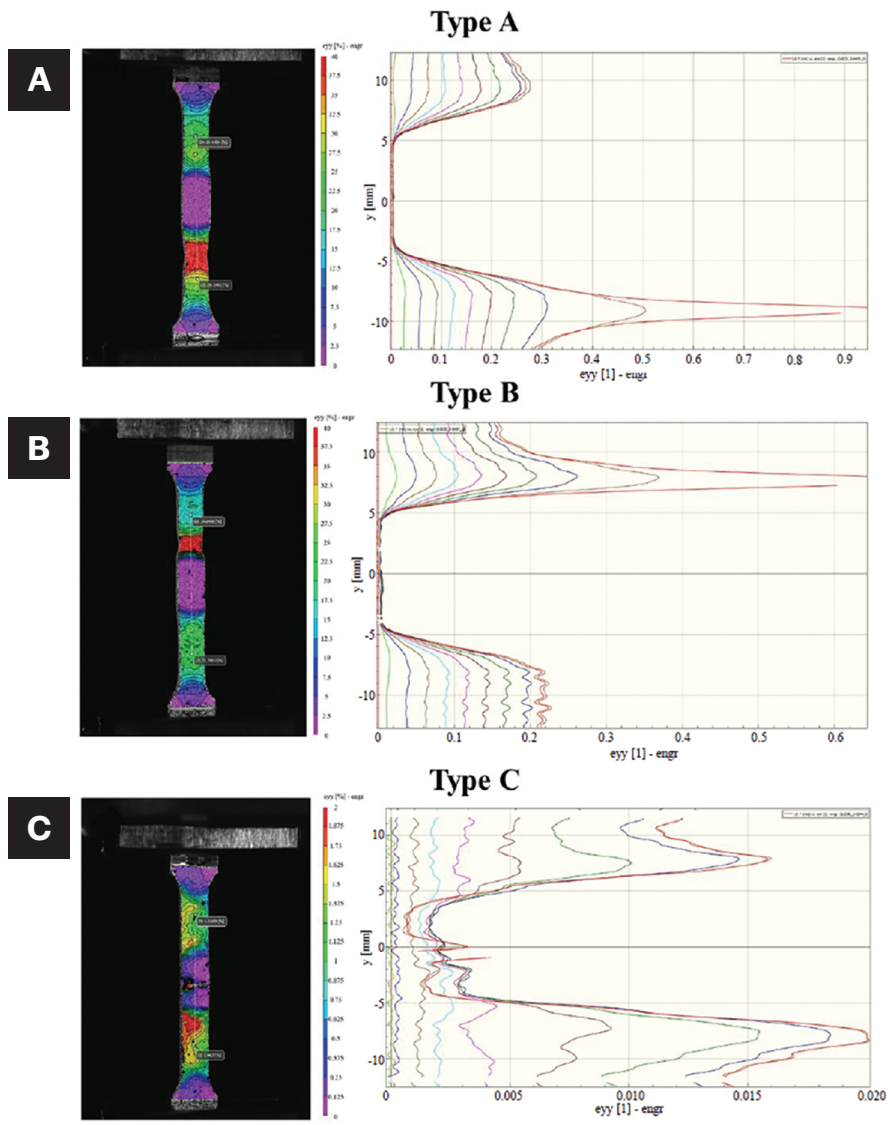


Fig. 14 — DIC obtained strain evolution curves for tensile coupons extracted from Gleeble welds: A — Type A samples; B — Type B samples; C — Type C samples at the onset of failure.

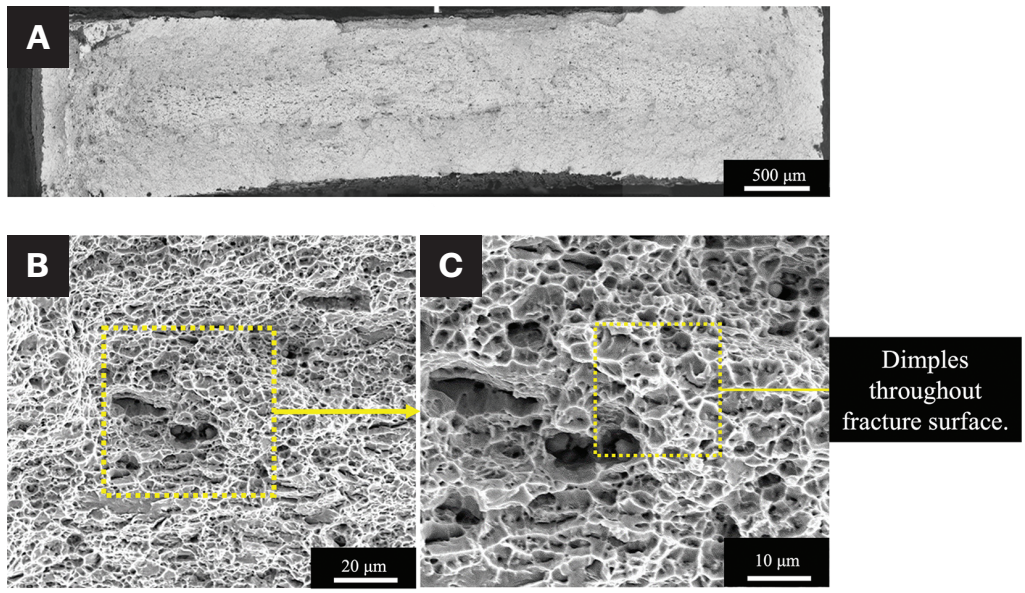


Fig. 15 — Fracture surface of Type A fracture showing the: A — Overall fracture surface and regions at: B — 1000× magnification; C — 2000× magnification under SEM using secondary electron imaging.

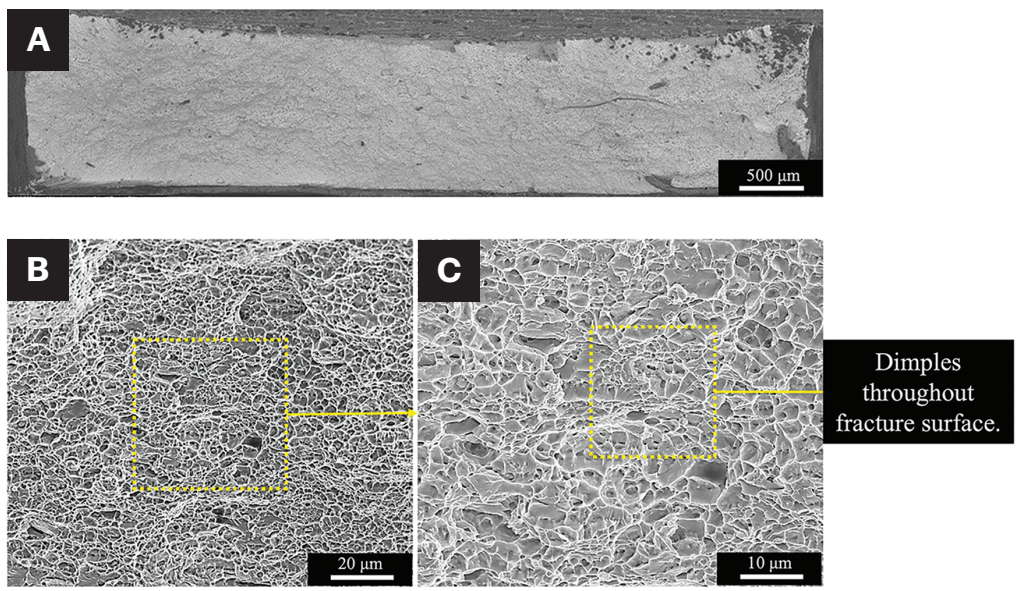


Fig. 16 — Fracture surface of Type B fracture showing the: A — Overall fracture surface and regions at: B — 1000× magnification; C — 2000× magnification under SEM using secondary electron imaging.

of samples failing with Type C fracture, instead, triple points where grain boundaries meet and the smooth planar surfaces of the grain boundaries are clearly visible (Fig. 17B), which is indicative of intergranular fracture. Closer inspection of the dark features showed that they were embedded between the grains (Fig. 17C). EDS mapping revealed that the dark features were oxide inclusions containing Al, Si and O (Fe was not identified in the features) as seen in Fig. 18. These oxide inclusions had similar chemical compositions to the oxide inclusions observed in other samples welded in the Gleeble. Such oxide inclusions can act as stress concentration points that have poor bonding with the surrounding metallic microstructure, serving as crack initiation sites, causing early failure and reduced ductility.

The fracture surface of the 3 HFIW tube samples that failed in the BL region during RHTT were also examined. SEM backscatter electron images showed that the BL fracture surfaces contained similar dark features to the Gleeble welds that failed in the BL (Type C) seen in Fig. 19A. These features were arranged in large through-thickness patches that were sparsely dispersed along the width of the weld. This trend differs from that observed in the Gleeble samples which had smaller patches dispersed along the entire surface of the bond line. EDS analysis confirmed that these dark features were Mn and Al containing oxides with Fe

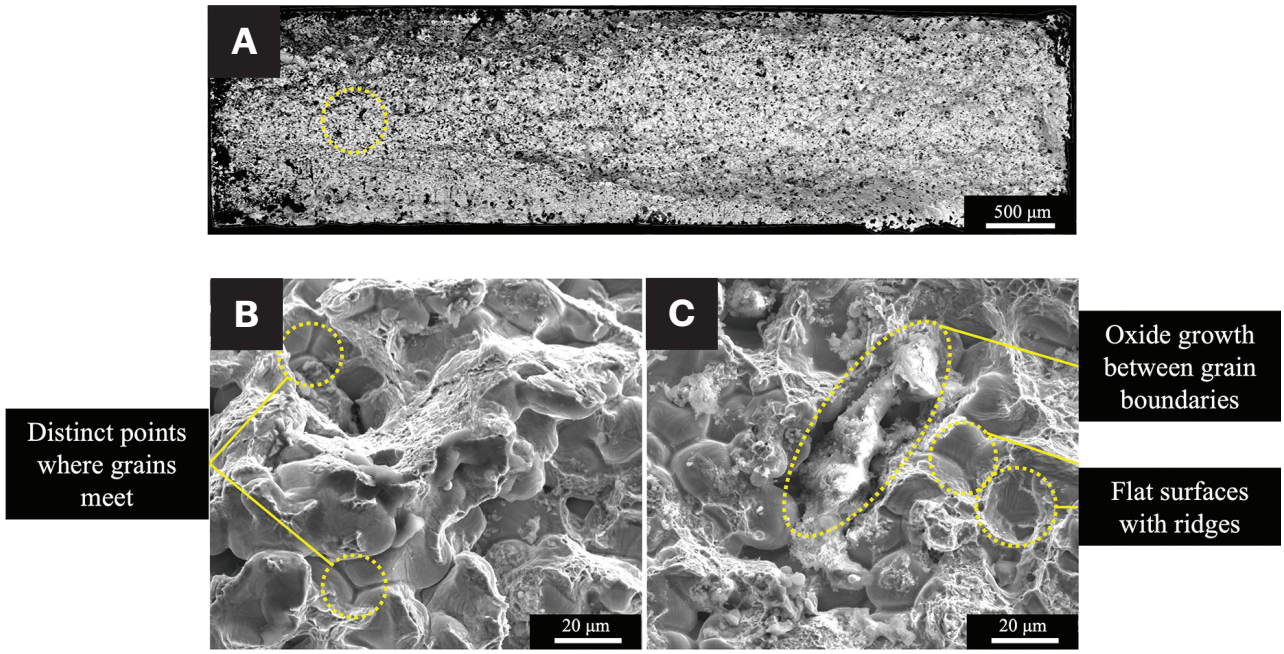


Fig. 17 — Fracture surface of Type C fracture showing the: A — Overall fracture surface; B — high magnification images showing the grain boundaries; and C — oxides between grains.

Table 3 — The UTS, Elongation, and Area Fraction Percent of Oxide Inclusions in Samples that Failed in the Bond Line

Sample	UTS (MPa)	Elongation (%)	% Area of Oxides
HFIW RHTT 1-1	760.6	10.8	1.0
HFIW RHTT 3-1	672.2	4.8	2.2
HFIW RHTT 4-2	630.8	2.0	4.6
Gleeble T9	458.9	1.0	10.3
Gleeble T10	347.5	0.4	13.6

content. In contrast to oxides found along the Gleeble BL, oxides from the HFIW had minimal Si. The differences seen in oxide distribution and composition found along the Gleeble and HFIW BL could be due to the continuous nature of the tubing process compared to the discrete nature of Gleeble welding. Oxide patches seen in the HFIW welds may have formed periodically, due to fluctuations of the HFIW process (i.e., periodic arcing), whereas in the Gleeble, the entire weld face would be simultaneously subjected to oxidation. The higher Si content of the oxides in the Gleeble may be due to it lower heating rate compared to the industrial HFIW process, 1000°C/s vs. ~ 15,000°C/s (as measured by the Xiris thermal camera), respectively. This means that the weld face in the Gleeble would be subjected to oxidation temperatures for longer, allowing for more elemental diffusion and oxide development. At a welding temperature of ~ 1400°C, the diffusivity of Mn in Fe is about 1×10^{-13} m^2/s, whereas it is about 5×10^{-14} m^2/s for Si in Fe (Ref. 38). It is reasonable to expect that oxides formed along the BL of HFIW would have less time to be enriched with Si due to elemental segregation. There was no lengthening of the gap or liquid metal ejection from the strip edges seen from the online monitoring of the HFIW process, nor were there any solidification structures seen in the area around the HFIW oxides. Therefore, it was concluded that these BL oxides are not penetrators, as penetrators are formed by the ejection of molten material ahead of the vee, which re-enters the bond line in an extended gap behind the vee (Refs. 39, 40).

Effect of Oxide Inclusions on Mechanical Properties

The area fraction of BL oxide on the fracture surface of the HFIW and Gleeble welds was measured to determine the effect of BL oxide on weld mechanical properties. To account

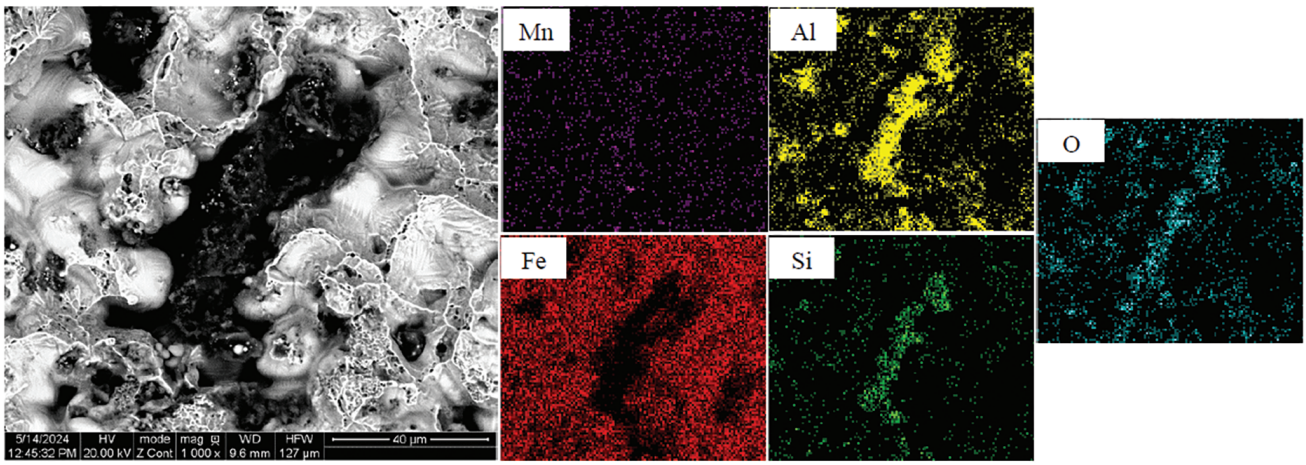


Fig. 18 — Backscatter SEM image of oxide from Fig. 17, along with EDS maps showing the Mn, Al, Fe, Si, and O of the region.

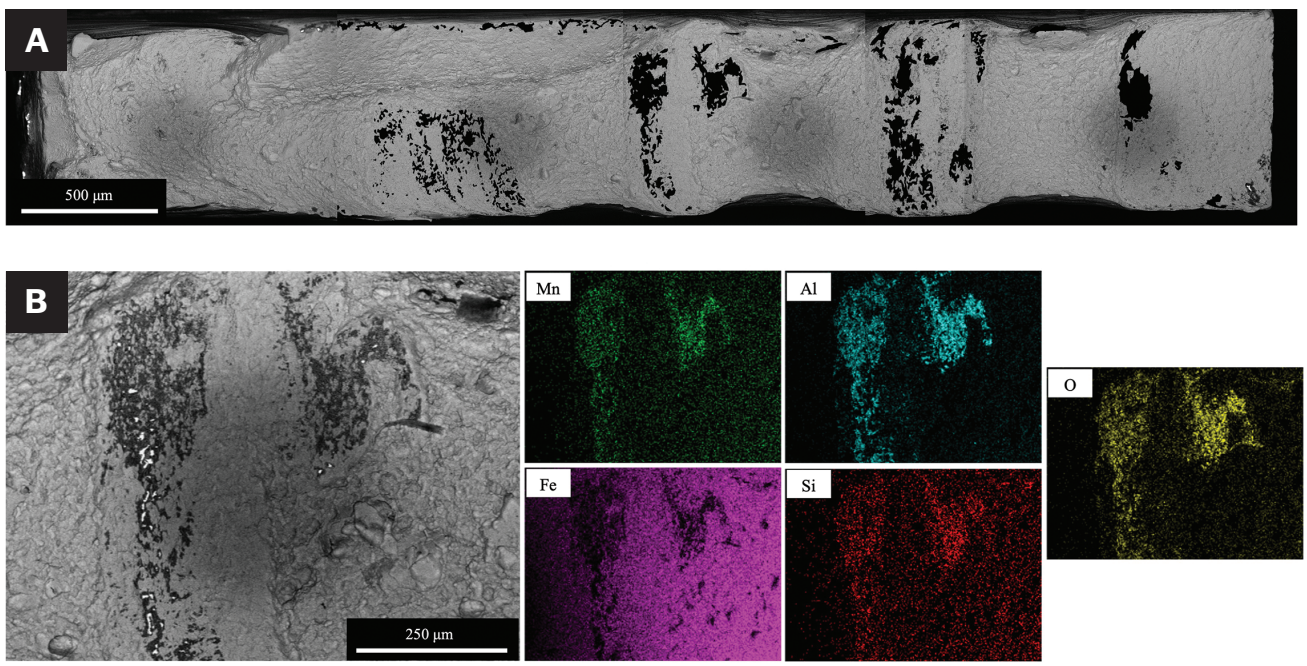


Fig. 19 — Fracture surface of tube sample which failed in BL showing the: A — Overall fracture surface; B — backscatter SEM image and EDS maps showing the Mn, Al, Fe, Si, and O of the region.

for differences in oxide distribution of the fracture surface in the two weld types, oxide area fraction was calculated using the entire fracture surface and 5 randomly selected areas of the fracture surface of the HFIW and Gleeble welds, respectively. The mechanical properties and respective oxide fractions for each weld are shown in Table 3. In both weld types, weld elongation was observed to decrease with an increase in the area fraction of present oxides.

Weld mechanical properties were graphed against BL oxide area fraction to determine if similar mechanical property-oxide area fraction trend exists in both weld types. In both the HFIW and Gleeble welds, the UTS and elongation decreased with increasing oxide area fraction. Specifically, a near approximate linear decrease of the UTS was observed with increasing oxide fraction (Fig. 20). The elongation property decreased sharply at low BL oxide content. However, the rate of elongation property decrease was slower with increase in present oxides.

Regression analysis was performed on the data set to better quantify the relationships between oxide area fraction and mechanical properties, as well as to confirm if observed trends are similar in both welding processes. The regression comparing UTS (σ_{UTS}) against the area fraction of the oxide inclusions (V_{oxide}) demonstrated a strong fit with an R^2 value of 98.7% and an adjusted R^2 value of 98.4% (Fig. 21). The residuals for the fit were both randomly distributed and showed no apparent grouping of the Gleeble and HFIW data, indicating the Gleeble and the HFIW strengths followed the same relation between mechanical properties and bond

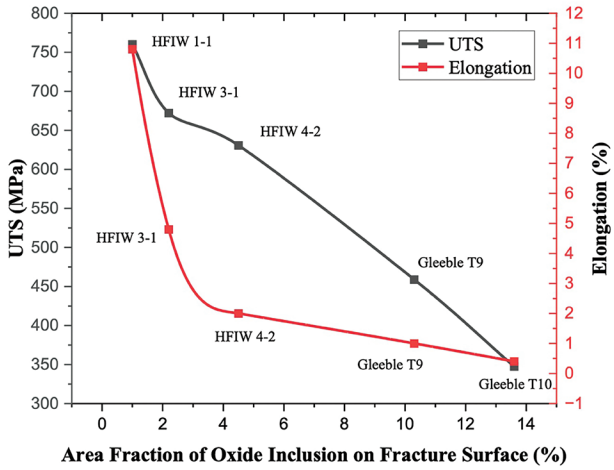


Fig. 20 — Changes in UTS and elongation with increased BL oxides for welds made using both the Gleeble and the HFIW.

line oxide content. The final relation between UTS and BL oxide content is:

$$\sigma_{UTS} = 768.0\ \text{MPa} - 30.7\ V_{oxide} \quad (1)$$

The elongation (ε) data was modelled as an exponential decay. This model fits the data very well with an R^2 value of 99.5% and an adjusted R^2 value of 98.9%, indicating a strong statistical fit. Also, the residuals were randomly distributed, and there was no grouping of the HFIW and Gleeble weld data. The equation relating elongation to oxide area fraction is (Fig. 21B shows a plot of the fitted exponential function):

$$\varepsilon = 0.8 + 20.3 \times e^{\frac{-V_{oxide}}{1.4}} \quad (2)$$

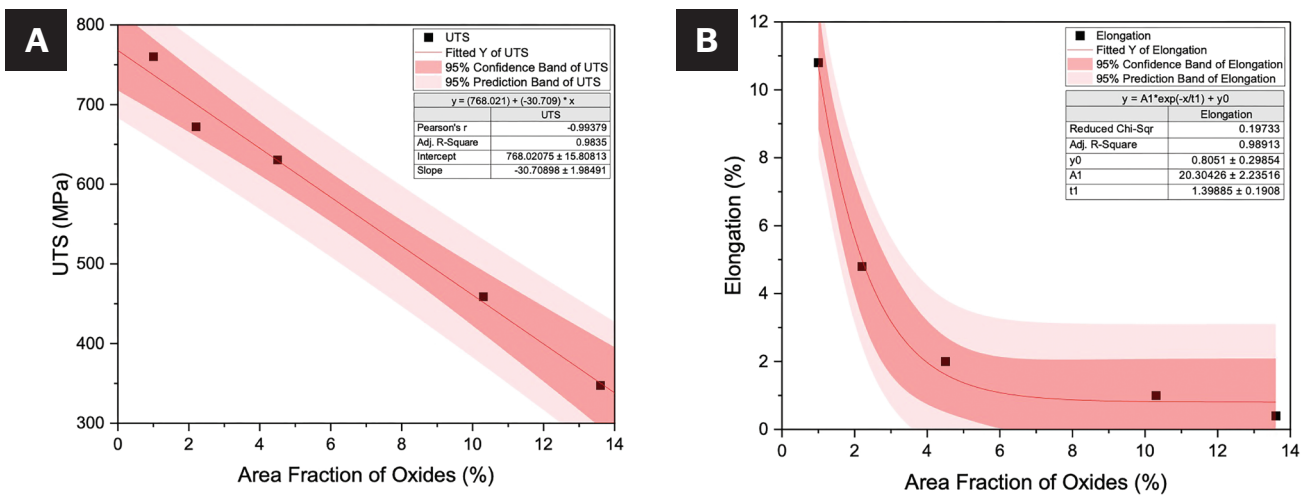


Fig. 21 — Statistical fit of the relation between: A — UTS; B — elongation with the area fraction of oxide inclusions for HFIW and Gleeble welds that failed in BL.

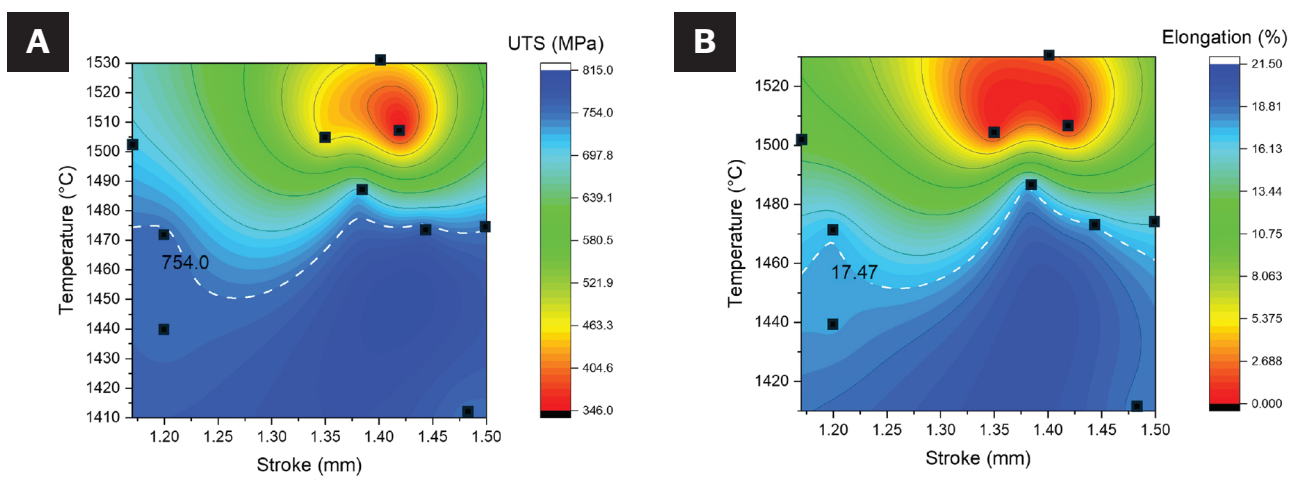


Fig. 22 — Process maps plotting Gleeble weld: A — UTS; B — elongation as a function of average BL temperature and stroke.

Process Map for Gleeble Parameters and Mechanical Performance

Tensile testing of Gleeble samples showed a large spread in strength and ductility across the different conditions. Defect-free welds failing in the BM exhibited high strength and elongation, while the welds containing oxide inclusions failed in the BL with significantly lower strength and elongation. Process maps have been created to understand how Gleeble process parameters, such as temperature and stroke, relate to measured mechanical properties. The dataset was transformed into an XYZ grid for plotting purposes using a gridding technique known as the Kriging method (Refs. 43, 44). This was important because the dataset contained only 10 randomly distributed points (due to difficulty controlling the BL temperature). The resulting process maps for UTS and elongation, shown in Fig. 22, show very similar trends.

At welding temperatures above ~ 1490°C, a sharp drop is observed in both the strength and ductility of the welded samples. This is due to the reduced strength and ductility of samples exhibiting Type C failure, which had peak temperatures above 1500°C. It should be noted that not all welds made with average peak temperatures exceeding 1500°C failed in the BL; some of these welds also exhibited Type B failure. The average UTS and elongation of Type A samples, which failed in the BM with high strength and ductility (highlighted by the white contour lines in Fig. 22) is predicted to be at BL welding temperatures between 1450°C and 1480°C, depending on the stroke. The values for both strength and elongation are predicted to be optimal at low to medium welding temperatures of 1410°C to 1460°C and a stroke range of 1.38 to 1.45 mm and 1.33 to 1.40 mm for UTS and elongation, respectively. The data shows that samples welded above a certain critical temperature are more likely to have lower mechanical properties. This critical temperature is likely related to the onset of melting, beyond which the BL becomes partially molten. All four samples, which were welded at temperatures above 1500°C, failed with lower strength and ductility, and all remaining samples, welded at temperatures below 1486°C, failed in the BM with high strength and ductility. Although this result seems surprising, considering that the solidus temperature of the material was 1472°C, it should be remembered that the temperature was measured from the top surface of the sample, which would have a slightly lower temperature than that of the bond face. Even considering this under-measurement of the welding temperature, this data is considered relevant to HFIW process control, as welding temperatures during industrial welding are measured from the top surface of the weld vee, and would have a similar under-measurement.

Conclusion

This study developed methods to perform laboratory-scale simulation of the HFIW of a thin TRIP 690 sheet using a Gleeble 3500, a technique that was only applied for heavy plate welds in the past. Furthermore, for the first time, this study validated the microstructure, fracture morphology, and mechanical property behavior of Gleeble-simulated welds against industrial HFIW welds. Gleeble-welded samples recreated both the microstructure and the mechanical properties of production HFIW welds. Furthermore, the welding results from the Gleeble gave insights into appropriate welding temperatures to achieve defect-free welds. Successful simulation of the HFIW process using a Gleeble provides a more cost-effective (lower operational costs and material usage) and time-efficient alternative to tube mill trials for developing the robust welding practices essential for industrial production of thin-walled Al-TRIP 690 HFIW tubes. The following major conclusions were obtained through this study:

- Gleeble welding can reproduce HAZ and BL microstructures observed in HFIW welded samples. SEM microscopy revealed that welds created in both the Gleeble and HFIW tube samples had microstructures consisting of ferrite, martensite, and tempered martensite in the BL and microstructures consisting mainly of martensite in the HAZ. However, the weld width of Gleeble-welded samples is three times as wide in comparison with the welds in HFIW tubes. This is because of the significantly lower frequency (60 Hz) of resistance heating used in the Gleeble. Regression analysis also showed that BL temperature significantly affected weld width in Gleeble-welded samples, with weld width increasing with increasing temperature.
- Hardness profiles of the Gleeble and HFIW welded samples were observed to be similar, with the hardness peaking within the HAZ, once differences in weld dimensions were accounted for. Also, the Gleeble welds exhibited a similar BL hardness drop seen in HFIW. In comparison with HFIW samples, the average BM hardness was 12.4% lower, and the HAZ hardness was 4.7% lower in Gleeble-welded samples. Increased hardness of the HFIW samples was due to work hardening of the tubes during roll forming. The increased dislocation density due to work hardening in the fin pass stand sections of the tube forming process likely resulted in metallurgical changes (either reduced grain size or increased dislocation density), hence an increase in hardness of the HAZ. No significant difference was observed between the BL hardness of the Gleeble and HFIW samples.
- Gleeble welding can reproduce welds containing oxide inclusions in the BL. EDS mapping showed that the oxide inclusions found in Gleeble welds contained mainly Si and Al, while oxide inclusions found in HFIW contained mainly Mn and Al. This difference in chemical composition was due to the longer heating times in Gleeble welding.
- Tensile testing showed that samples containing oxide inclusions along the BL failed in the BL with significantly reduced strength and ductility in both Gleeble welding and HFIW. Statistical analysis showed that oxides affect the strength of the Gleeble and HFIW welds similarly. The UTS was observed to decrease linearly with increased BL oxide, while elongation decreased sharply at low oxide contents, followed by a less rapid decline with increasing BL oxide presence.
- Tensile testing results were used to create process maps of the mechanical properties across different welding conditions for Gleeble welding. The process maps showed that strength and ductility both decreased significantly in samples welded above ~ 1490°C, due to the formation of BL oxides. Meanwhile, samples welded at BL welding temperatures below 1486°C failed in the base metal, with high strength and elongation, and the process maps predicted BL welding temperatures of 1410°C to 1460°C, with a stroke of 1.33 to 1.45 mm, as ideal for maximizing strength and ductility.

Acknowledgments

The authors thank ArcelorMittal Dofasco, the Natural Sciences and Engineering Research Council of Canada (NSERC), and Mitacs (through the Mitacs Accelerate Program) for their financial support of this project.

References

1. Curtis, F. W. 1944. High-frequency induction heating. McGraw-Hill Book Co. New York, N.Y.

2. Yan, P., Güngör, O. E., Thibaux, P., Liebeherr, M., and Bhadeshia, H. K. D. H. 2011. Tackling the toughness of steel pipes produced by high frequency induction welding and heat-treatment. *Materials Science and Engineering A* 528(29–30): 8492–8499. DOI: 10.1016/j.msea.2011.07.034

3. Ravikiran, K., Xu, P., and Li, L. 2024. A critical review on high-frequency electric-resistance welding of steel linepipe. *Journal of Manufacturing Processes* 124: 753–777. DOI: 10.1016/j.jmapro.2024.06.046

4. Wright, J. 1997. Principles of high frequency induction tube welding. Electronic Heating Equipment Inc.

5. Tisza, M. 2021. Three generations of advanced high strength steels in the automotive industry. Lecture Notes in Mechanical Engineering 22: 81–94.

6. Fonstein, N. 2015. Advanced high strength sheet steels: Physical metallurgy, design, processing, and properties. Springer International.

7. Soleimani, M., Kalhor, A., and Mirzadeh, H. 2020. Transformation-induced plasticity (TRIP) in advanced steels: A review. *Materials Science and Engineering A* 795: 140023. DOI: 10.1016/j.msea.2020.140023

8. Oliver, S., Jones, T. B., and Fourlaris, G. 2007. Dual phase versus TRIP strip steels: Comparison of dynamic properties for automotive crash performance. *Materials Science and Technology* 23(4): 423–431.

9. Grajcar, A., Rózański, M., Kamińska, M., and Grzegorczyk, B. 2014. Study on non-metallic inclusions in laser-welded TRIP-aided Nb-microalloyed steel. *Archives of Metallurgy and Materials* 59(3): 1163–1169. DOI: 10.2478/amm-2014-0203

10. Amirthalingam, M., and Hermans, M. J. M. 2009. Microstructural development during welding of silicon- and aluminum-based transformation-induced plasticity steels—Inclusion and elemental partitioning analysis. *Metallurgical and Materials Transactions A* 40(4): 901–909. DOI: 10.1007/s11661-008-9761-5

11. Park, G., Jeong, S., Kang, H., and Lee, C. 2018. Improvement of circumferential ductility by reducing discontinuities in a high-Mn TWIP steel weldment. *Materials Characterization* 139: 293–302. DOI: 10.1016/j.matchar.2018.03.009

12. Egger, C., Kroll, M., Kern, K., Steimer, Y., Schreiner, M., and Tillmann, W. 2022. Experimental investigation of temperature and contact pressure influence on HFI welded joint properties. *Materials* 15(10): 1–18. DOI: 10.3390/ma15103615

13. Haga, H., Aoki, K., and Sato, T. 1980. Welding phenomena and welding mechanisms in high frequency electric resistance welding—1st report. *Welding Journal* 59(7): 208s–212s.

14. Ghaffarpour, M., Akbari, D., and Naeini, H. M. 2021. Investigation on the effects of the joint type on the driven out bead in the welded pipes produced by high-frequency induction welding. *Proceedings of the Institution of Mechanical Engineers Part L: Journal of Materials: Design and Applications* 235(3): 597–612.

15. Asperheim, J. I., Das, P., Grande, B., and Hömberg, D. 2024. Numerical simulation of high-frequency induction welding in longitudinal welded tubes. *Journal of Mathematics in Industry* 14: 21. DOI: 10.1186/s13362-024-00147-8

16. Kim, H. J., and Youn, S. K. 2008. Three dimensional analysis of high frequency induction welding of steel pipes with impeder. *Journal of Manufacturing Science and Engineering* 130(3): 0310051–0310057. DOI: 10.1115/1.2844586

17. Han, Y., and Yu, E. L. 2012. Numerical analysis of a high-frequency induction welding process. *Welding Journal* 91(10): 270s–277s.

18. Ghaffarpour, M., Akbari, D., Naeeni, H. M., and Ghanbari, S. 2019. Improvement of the joint quality in the high-frequency induction welding of pipes by edge modification. *Welding in the World* 63(6): 1561–1572. DOI: 10.1007/s40194-019-00779-0

19. Yang, F., Wen, T., Wang, Q., Zhang, L., Liu, H., and Zhou, Y. 2024. Effect of high-frequency induction weld seam on the deformation of M1700 ultra-high strength steel shell structures considering residual tensile stress. *Thin-Walled Structures* 195: 111340. DOI: 10.1016/j.tws.2023.111340

20. Mishra, A., and Pal, S. 2020. Electromagnetic transient-thermal modeling of high-frequency induction welding of mild steel plates. *Advances in Simulation, Product Design and Development* 407–415. DOI: 10.1007/978-981-32-9487-5

21. Han, Y., Yu, E. L., and Zhao, T. X. 2016. Three-dimensional analysis of medium-frequency induction heating of steel pipes subject to motion factor. *International Journal of Heat and Mass Transfer* 101: 452–460. DOI: 10.1016/j.ijheatmasstransfer.2016.05.017

22. Han, Y., Yu, E., Huang, D., and Zhang, L. 2014. Simulation and analysis of residual stress and microstructure transformation for post weld heat treatment of a welded pipe. *Journal of Pressure Vessel Technology* 136: 021401. DOI:10.1115/1.4025942

23. Han, S. -W., Kang, S. -C., Yi, J., and Kim, H. -K. 2018. Prediction of mechanical properties of ERW pipes considering manufacturing process through numerical analysis. *Proceedings of the 12th International Pipeline Conference* IPC2018-78491.

24. Santana, I. J., Paulo, B., and Modenesi, P. J. 2006. High frequency induction welding simulation on ferritic stainless steels. *Journal of Materials Processing Technology* 179: 225–230. DOI: 10.1016/j.jmatprotec.2006.03.063

25. Kannan, R., Li, L., Guo, L., Anderson, N., Rashid, M., Collins, L., and Arafin, M. 2020. Bond formation mechanism for resistance welding of X70 pipeline steel. *Welding Journal* 99(8): 209s–223s. DOI: 10.29391/2020.99.020

26. Yurioka, N., Suzuki, H., Ohshita, S., and Saito, S. 1983. Determination of necessary preheating temperature in steel welding. *Welding Journal* 62(6): 147s–153s.

27. Kim, J., Shojaee, M., Ramachandran, D.C., Betiku, O. T., Ghassemi-Armaki, H., and Biro, E. 2025. A novel in-situ temperature measurement method for liquid metal embrittlement cracking analysis. *Science and Technology of Welding and Joining*: 1–9. DOI: 10.1177/13621718251389304

28. Biro, E., and Lowes, K. 2014. High frequency induction tube welding parameters for OCTG applications. *Proceedings of CANWELD* 2014.

29. Varbai, B., Nagy, E., Kristály, F., Mertinger, V., and Adonyi, Y. 2022. What are ERW bond lines? *Tube and Pipe Journal*.

30. ASTM International. 2017. Standard test method for microindentation hardness of materials. ASTM Standard E384: 1–40.

31. ASTM International. 2013. Standard test methods for tension testing of metallic materials. ASTM Standard E8/E8M-13a. DOI: 10.1520/E0008_E0008M-13a

32. Calaf-Chica, J., Martínez-Peña, J., Miguel, P., Díez, B., and Calzada, M. P. 2022. Ring hoop tension test for yield strength estimation: Numerical analysis for a novel correlation method and applicability for mechanical testing of tubes. *Mechanics of Materials* 169: 104295. DOI: 10.1016/j.mechmat.2022.104295

33. Khalfallah, A., Ktari, Z., Leitão, C., and Fernandes, J. V. 2021. New mandrel design for ring hoop tensile testing. *Experimental Techniques* 45: 769–787. DOI: 10.1007/s40799-021-00462-4

34. Dick, C. P., and Korkolis, Y. P. 2014. Mechanics and full-field deformation study of the ring hoop tension test. *International Journal of Solids and Structures* 51(18): 3042–3057. DOI: 10.1016/j.ijsolstr.2014.04.023

35. Okoroafor, S. 2024. A study on high-frequency induction welding of TRIP 690 tubes using mechanical tests and computer simulations. MASc Thesis, University of Waterloo, Waterloo, Canada.

36. Sharma, N. K., Kannan, R., Li, L., Anderson, N., Rashid, M., Collins, L., Poplawsky, J. D., and Unocic, R. 2021. A mechanism for carbon depletion at bondline of high-frequency electric-resistance-welded X70 pipeline steel. *Metallurgical and Materials Transactions A* 52(9): 3788–3798. DOI: 10.1007/s11661-021-06339-w

37. Wulpi, D. J. 2013. Understanding how components fail. ASM International.

38. Oikawa, H. 1983. Lattice diffusion of substitutional elements in iron and iron-base solid solutions: A critical review. *Technology Reports of Tohoku University* 48(1): 7–77.

39. Haga, H., Aoki, K., and Sato, T. 1981. Mechanisms of formation of weld defects in high-frequency electric resistance welding. *Welding Journal* 60(6): 104s–109s.

40. Kim, C., and Kim, J. 2009. The effect of heat input on the defect phases in high frequency electric resistance welding. *Metals and Materials International* 15(1): 141–148. DOI: 10.1007/s12540-009-0141-5

41. Gale, W. F., and Totemeier, T. C., eds. 2004. Smithells metals reference book. 8th ed. Elsevier Butterworth-Heinemann.

42. Klug, F. J., Prochazka, S., and Doremus, R. H. 1987. Alumina–silica phase diagram in the mullite region. *Journal of the American Ceramic Society* 70(10): 750–759. DOI: 10.1111/j.1151-2916.1987.tb04875.x

43. Cressie, N. 1990. The origins of kriging. *Mathematical Geology* 22(3): 239–252. DOI: 10.1007/BF00889887

44. Oliver, M.A., and Webster, R. 2014. A tutorial guide to geostatistics: Computing and modelling variograms and kriging. *Catena* 113: 56–69. DOI: 10.1016/j.catena.2013.09.006

SYED FAIQUE AL HUSSAIN, AHAD SHAFIEE, SYDNEY OKOROAFOR, DILEEP CHANDRAN RAMACHANDRAN, ADIB SALANDARI-RABORI, MOHAMMAD SHOJAEE, and **ELLIOT BIRO** (*elliot.biro@uwaterloo.ca*) are with the Centre for Advanced Materials Joining (CAMJ), Department of Mechanical & Mechatronics Engineering, University of Waterloo, Waterloo, Canada. **DANIEL ODOH** is with ArcelorMittal Global R&D Hamilton, Hamilton, Canada.